scientific reports

OPEN

Double effects of O_2 on passive film of super 13Cr stainless steel in CO_2 saturated environment

Lv Naixin[1], Fu Anqing[1✉], Yu Haitao[2], Zhang Gang[2], Wei Chenghua[3], Wang Xia[4], Xu Zhengyi[1,5,6,7✉] & Wang Yanqiu[5]

Herein, a comprehensive suite of electrochemical methods, including cyclic polarization, Mott-Schottky (M-S), and electrochemical impedance spectroscopy (EIS) tests, were employed to investigate the effects of O_2 on passivation and pitting behavior of Super 13Cr in CO_2-saturated environment. Our findings reveal that O_2 plays a dual role: O_2 substantially enhances the stability of passive film by diminishing point defeat density, thereby improving the resistance to local corrosive attacks. Conversely, within the stable pitting domain, O_2 exacerbates the severity of the corrosive environment, undermining the repassivation capabilities of super 13Cr stainless steel. The study elucidates the intricate interplay of O_2 and the passive film, offering valuable insights for the strategic application of Super 13Cr in the demanding conditions of modern oil and gas extraction processes where CO_2 and O_2 coexist.

The insatiable global demand for energy has spurred the development of advanced oil and gas recovery techniques aimed at enhancing extraction efficiency[1,2]. However, these advanced exploration and production methods have also introduced significant corrosion challenges to downhole tubing and surface gathering pipeline systems, primarily due to the harsh environmental conditions encountered[3]. Stainless steels, known for their excellent mechanical properties, cost-effectiveness, and strong resistance to CO_2-induced corrosion, have become the preferred materials for these critical applications[4]. Extensive researches have investigated the corrosion behavior of stainless steels under various environmental conditions[5–7], revealing that the uniform corrosion rate of stainless steels increases with rising temperatures and CO_2 partial pressure[8,9]. Particularly under extreme service conditions, such as 180 °C and 4.16 MPa P_{CO_2}, the corrosion rate significantly increases, and the incidence of pitting corrosion becomes more pronounced[10].

The susceptibility of metals to corrosion is inherently governed by the characteristics of protective oxide layers that develop on surfaces, especially in highly aggressive environments[11–13]. The properties of corrosion product layers, i.e., composition and structure, are significantly influenced by environmental factors[14,15]. With the advent of polythermal fluid injection and aerated methods to enhance reservoir productivity, oxygen (O_2) has been introduced into downhole conditions, shifting the traditional corrosion condition from a CO_2-dominated environment to a mixed O_2/CO_2 atmosphere[16–18]. The transition, coupled with the increasing depths of drilling operations and the consequent rise in downhole temperature and pressure, has further complicated the service environment for tubing and exacerbated the severity of service conditions. Field observations have reported incidents of corrosion-induced perforation and catastrophic tubing failures within the O_2/CO_2 coexistence environment[19,20]. Li et al.[21] documented that impurities can mitigate corrosion rates and nodule proliferation, thereby enhancing the stability of chromium oxides. However, Bouhieda et al.[22] argued that these impurities could accelerate the early development of a protective chromium-rich oxide layer. The finding contrasts with the work of Mahaffey et al.[23], who identified that the same levels of oxygen impurities can increase the likelihood of nodular defects and internal oxidation, as well as the formation of voids in the matrix, attributed to the

[1]State Key Laboratory of Oil and Gas Equipment, CNPC Tubular Goods Research Institute, Xi'an 710077, China. [2]Longdong Oil and Gas Development company of Changqing Oil field, Qingyang 745000, China. [3]Xi'an Changqing Engineering Construction Supervision Co.,Ltd, Xi'an 710016, China. [4]Associated Gas Comprehensive Utilization Department of Changqing Oil field, Xi 'an 710016, China. [5]International Joint Laboratory of Advanced Bulk Nanomaterials for Innovative Applications, Harbin Engineering University, Harbin 150001, China. [6]CEPREI, Guangzhou 511370, China. [7]Guangzhou Provincial Key Laboratory of Electronic Information Products Reliability Technology, Guangzhou 511370, China. ✉email: fuanq@cnpc.com.cn; xuzhengyi@hrbeu.edu.cn

accelerated outward diffusion of chromium. These conflicting results highlight the complex role of impurities in the formation and stability of chromium oxides, which is a key consideration in the context of the work.

The study addresses the passivation and pitting mechanism gap of Super 13Cr under 50% N_2/O_2 + 50% CO_2 environment by employing a comprehensive array of electrochemical assays and artificial pitting electrode experiment. The study aims to elucidate the significant effects of oxygen on passive film, utilizing the Point Defect Model (PDM)[24,25] and Galvele's local acidification theory[26] as theoretical frameworks. Our findings underscore the pivotal role of O_2 in enhancing the passive film stability and intensifying corrosiveness of local environment within pits, providing a theoretical foundation for ensuring the reliable service life of oil pipeline materials in the challenging environments encountered in unconventional oil and gas extraction operations.

Experimental

Materials

Super 13Cr martensitic stainless steel (chemical composition detailed in Table 1) was utilized. Electrochemical test specimens were prepared as squares ($10 \times 10 \times 3$ mm), sealed, and an area of 10×10 mm was exposed for testing. Additionally, an artificial pitting electrode was fabricated from a small round rod with a diameter of 350 μm, resulting in an active area of 9.6 mm². A 0.1 M NaCl solution, prepared using 99.9% pure reagents and deionized water, was used for electrochemical testing. The experimental gas mixtures consisted of 50% O_2 + 50% CO_2 and 50% N_2 + 50% CO_2. The dissolved oxygen levels in the solutions equilibrated with gas mixtures were 0.3 and 12.6 mg/L, measured using a HACH dissolved oxygen electrode (LDO10101). Both saturated solutions exhibited a pH of 4.2, and the measurements were conducted at 25 ℃. Before electrochemical experiments, deoxygenation process was employed by purging with the mixture gas for 2 h.

Electrochemical measurements

Electrochemical experiments were conducted using the P4000 A potentiostat from Princeton Applied Research, with a standard three electrode setup (counter electrode: platinum sheet, reference electrode: solid Ag/AgCl electrode (−0.221 V, in our previous work[27]). Specimens were carefully prepared using SiC sandpaper up to 1500 grit, followed by thorough rinsing and decontamination. To remove the native surface oxide film, the specimens were polarized at −1 V vs. open circuit potential (OCP) for 5 min. The system was then allowed to stabilize for 1 h before tests. Cyclic potentiodynamic polarization tests commenced at −0.15 V vs. OCP with the scan rate of 0.333 mV·s⁻¹. Reverse scan was initiated once the current density exceeded 1×10^{-3} A·cm⁻². For potentiostatic polarization, samples were held at constant film-forming potentials (E_f) of −0.16, −0.08, 0 and 0.08 V for 2 h to generate polarization curves. Subsequent to polarization, measurements of EIS were performed using a 10-mV amplitude across a frequency spectrum extending from 10^{-2} to 10^5 Hz. Directly following the potentiostatic polarization, a Mott-Schottky (M-S) test was executed. The test started from the polarization potential and descended to −0.5 V in steps of −0.02 V.

Results

Cyclic potentiodynamic polarization curves

Figure 1 illustrates the cyclic potentiodynamic polarization results for Super 13Cr in 0.1 M NaCl solution under the two environments: 50% O_2 + 50% CO_2 and 50% N_2 + 50% CO_2, which has explained in our previous study[28]. The parameters are detailed in Table 2. In both environments, Super 13Cr stainless steel demonstrates passivation behavior during anodic polarization. The corrosion potential (E_{corr}) is indicative of the passive film stability[29]. Higher E_{corr} observed in the 50% O_2 + 50% CO_2 environment suggests enhanced passive film stability, as evidenced by lower passivation current density (i_p).

The pitting potential (E_b) is a critical parameter marking the threshold at which the metastable pitting transitions to stable pitting in stainless steel[30]. Repassivation potential (E_p) defines a critical threshold for pitting growth[31]. Below E_p, pitting is unlikely to occur, whereas above it, metastable pitting can initiate, and existing stable pitting may propagate. A larger difference (ΔE) between E_b and E_p indicates greater susceptibility to passive film damage and reduced self-repair capacity[32]. In the 50% O_2 + 50% CO_2 environment, Super 13Cr stainless steel exhibits higher E_b and lower E_p, leading to a larger ΔE. This suggests that passive film is chemically more stable in the O_2 + CO_2 environment, while once stable pitting initiates, repassivation becomes more challenging.

Potentiostatic polarization curves

Based on the cyclic potentiodynamic polarization curve tests (Fig. 1), potentiostatic polarization was conducted at different E_f within the complete passivation region (E_{corr} to E_p): −0.16, −0.08, 0 and 0.08 V. The tests were performed in a 50% O_2/N_2 + 50% CO_2 environment for 2 h, as depicted in Fig. 2. As demonstrated in Fig. 2(a-d), the potentiostatic polarization curves exhibit a pronounced initial decrease in current density, which can be attributed to the rapid formation and growth of the passive film. Over time, the current density on all polarization curves tended toward stabilized as the rates of passive film formation and dissolution reached equilibrium. The absence of prominent current peaks in the curves indicates that metastable pitting did not occur at any applied E_f values for Super 13Cr.

Element	C	Ni	Cr	Si	Mo	P	S	Mn	Fe
Content	0.027	5.32	12.87	0.18	2.20	0.022	0.004	0.47	Bal.

Table 1. Chemical composition of experimental super 13Cr (wt%).
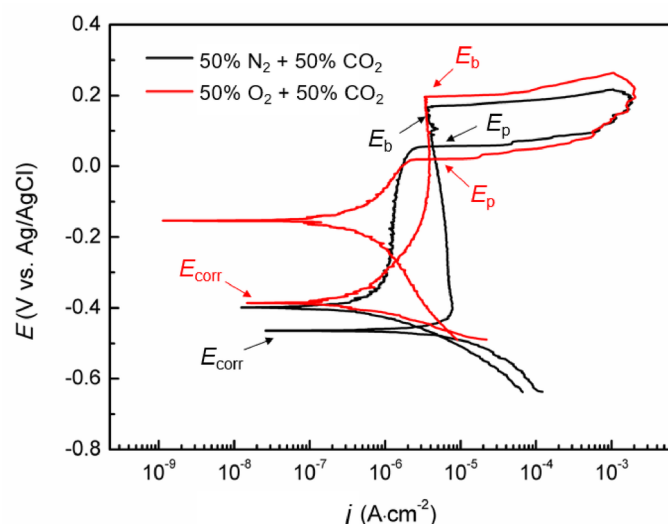
Fig. 1. Cyclic potentiodynamic polarization results of Super 13Cr under a 50% N_2/O_2 and 50% CO_2 environment.

Environment	E_{corr} (V)	i_p (A·cm^{-2})	E_b (V)	E_p (V)	$\Delta E = E_b - E_p$ (V)
50%N_2 + 50%CO_2	−0.466	5.32×10^{-6}	0.235	0.107	0.128
50%O_2 + 50%CO_2	−0.215	3.06×10^{-6}	0.253	0.901	0.163

Table 2. Key parameters obtained in Fig. 1.

Figure 2(e) displays the steady-state current densities (i_{ss}) at various E_f. For n-type passive film with metal interstitial ions and oxygen vacancies as the predominant point defects, the passivation current density is anticipated to be unaffected by the E_f[33]. The data in Fig. 2(e) reveal that, regardless of the gaseous environment, the i_{ss} of Super 13Cr remains constant, which suggests that the passive films formed under both environments share the same n-type semiconductor characteristics.

EIS tests

Figure 3 displays the EIS results of Super 13Cr stainless steel after potentiostatic polarization. The impedance arc radius for Super 13Cr increases with increasing E_f, indicating enhanced protection. Impedance data were analyzed with the equivalent electrical circuit (EEC) inserted in the Nyquist plots (Fig. 3a, c)[34–36], and summarized in Table 3. R_s and R_{ct} denote the solution and charge transfer resistance[37], CPE_f corresponds to the passive film capacitance. At a given E_f, the R_{ct} of Super 13Cr in the 50% O_2 + 50% CO_2 environment is higher than that in the 50% N_2 + 50% CO_2 environment, suggesting that oxygen significantly enhances passive film stability. The results align with the established understanding that passive film properties are pivotal in determining corrosion resistance of stainless steels, as supported by literature[33,38].

The formula is used to deduce the relationship between the thickness of the passive film (L_{ss}) and CPE_f[39–41]:

$$L_{ss} = \frac{\varepsilon_0 \, \varepsilon \, A}{CPE_f} \tag{1}$$

Here, ε_0 and ε are the vacuum permittivity (8.854×10^{-14} F·cm^{-1}) and dielectric constant (taken as 15.6[42]), and $A (= 1 \text{ cm}^2)$ is exposed specimen area. The calculated values of L_{ss} are compiled in Table 3 and are consistent with the thickness ranges reported in the literature. Our findings reveal that, for a given E_f, the L_{ss} in O_2 + CO_2 environment exceeds that formed in N_2 + CO_2 environment. The observation suggests that oxygen facilitates the development of the passivation, thereby enhancing passivation performance. The relationship between L_{ss} and E_f for Super 13Cr stainless steel was linear fitted (Fig. 4), and the correlation followed the equation[43]:

$$L_{ss} = \frac{1}{\varepsilon_L}(1 - \alpha)E_f + B \tag{2}$$

The average electric field strength (ε_L) was determined using polarization rate (α) at the passive film/solution interface, which is reported as 0.743[44]. The relationship is given by Eq. (2), where B is a constant specific to the system. The values of ε_L were calculated for the two different environments: 0.78×10^6 V·cm^{-1} for 50% O_2 + 50% CO_2 environment and 0.65×10^6 V·cm^{-1} for 50% N_2 + 50% CO_2 environment using this equation, suggesting that oxygen significantly enhances the ε_L within passive film on Super 13Cr stainless steel.
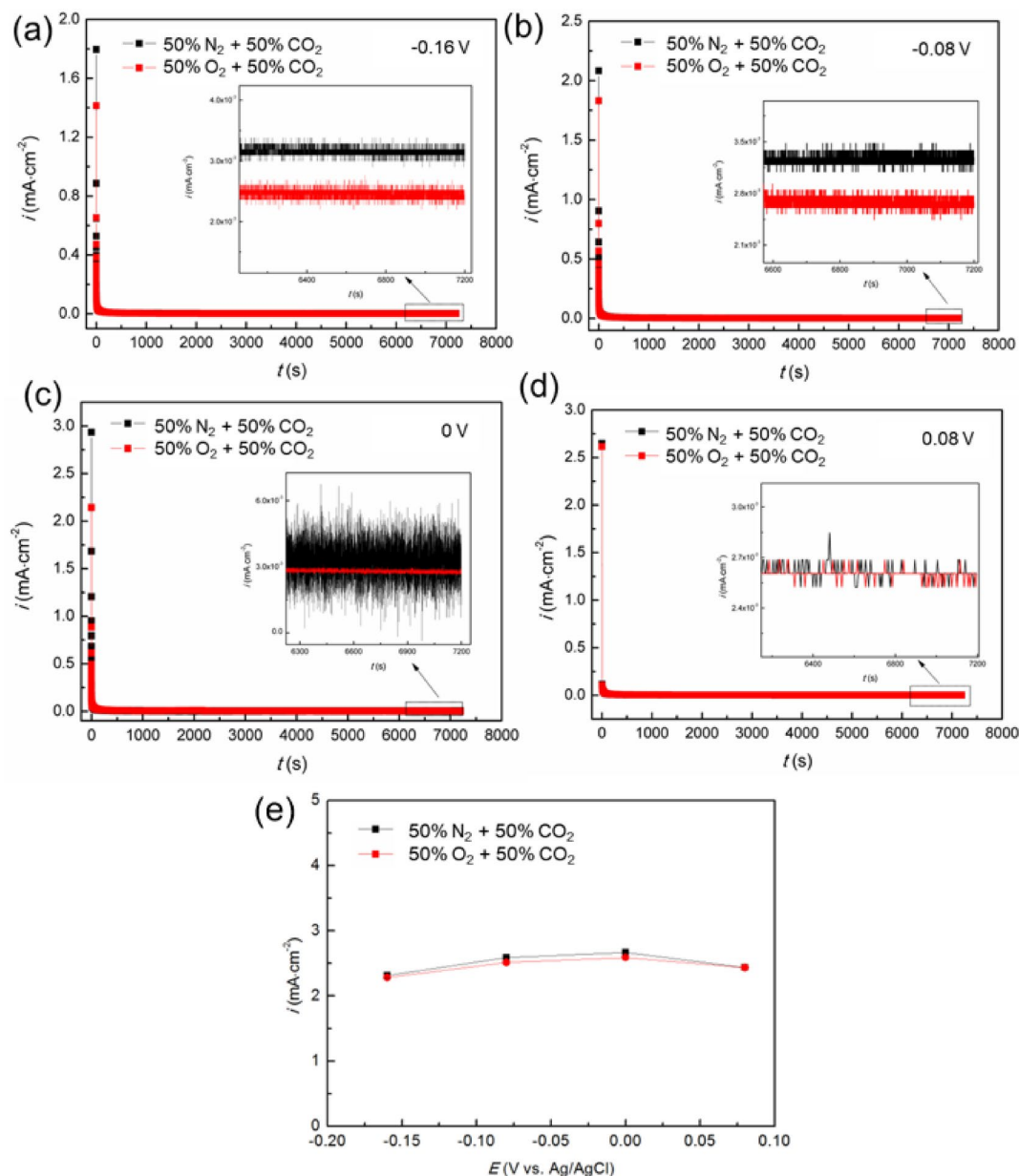
Fig. 2. Potentiostatic polarization curves of Super 13Cr at various E_f: (**a**) −0.16 V, (**b**) −0.08 V, (**c**) 0 V, and (**d**) 0.08 V for 2 h; (**e**) the correlation between i_{ss} and E_f.

M-S analysis

The PDM posits the semiconductor behavior of passive film. The susceptibility of the film to rupture, and consequently the initiation of pitting, is intrinsically connected with semiconductor properties. The space charge capacitance (C) and potential (E) are interrelated as follows:

$$\frac{1}{C^2} = \frac{2}{\varepsilon\varepsilon_0 e N_D}\left(E - E_f - \frac{kT}{e}\right) \qquad \text{n-type} \qquad (3)$$

$$\frac{1}{C^2} = -\frac{2}{\varepsilon\varepsilon_0 e N_A}\left(E - E_f - \frac{kT}{e}\right) \qquad \text{p-type} \qquad (4)$$

where e is the elementary charge (1.602×10^{-19} C), N_D and N_A represent the concentrations of donors and acceptors, respectively. E_{fb} is flat band potential, k denotes Boltzmann constant, and T represents absolute temperature. According to PDM, the passive film formed on stainless steel is considered as semiconductor oxide layer, filled with point defects that significantly influence the film's integrity and its susceptibility to pitting corrosion. The model delineates the passive film into two distinct layers: inner barrier and outer precipitation
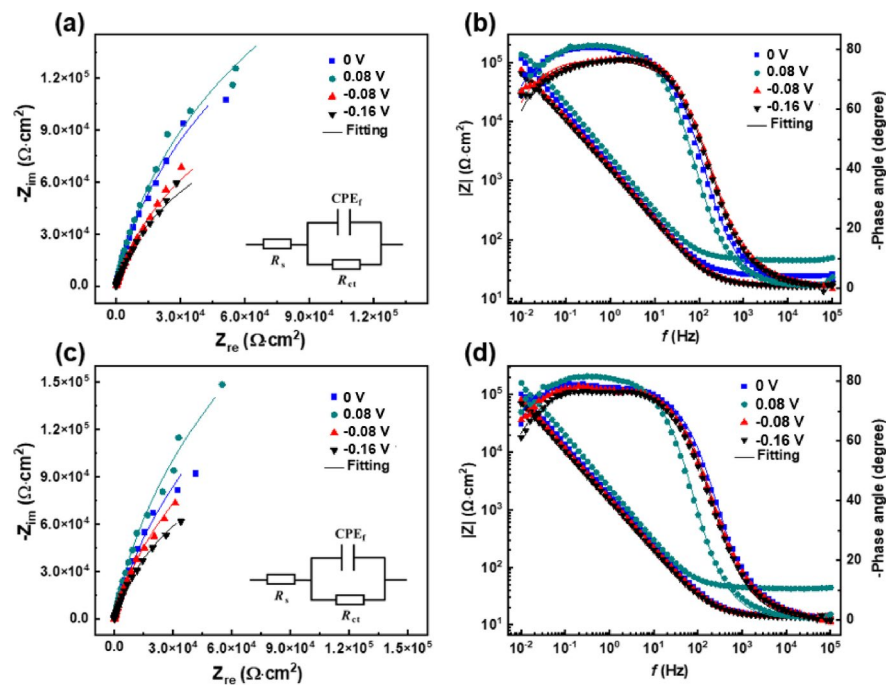
Fig. 3. EIS results of Super 13Cr under various environments: (**a, b**) 50% N_2 + 50% CO_2, (**c, d**) 50% O_2 + 50% CO_2; (**a, c**) Nyquist plots and (**b, d**) Bode plots.

Conditions	E_f (V)	R_s ($\Omega \cdot cm^2$)	R_{ct} (10^4 $\Omega \cdot cm^2$)	C_f (10^{-5} $F \cdot cm^{-2}$)	n	L_{ss} (nm)
50%N_2 + 50%CO_2	−0.16	13.23	17.53	1.73	0.86	0.61
	−0.08	13.38	22.92	1.60	0.86	0.69
	0	13.62	39.41	1.25	0.9	0.89
	0.08	13.52	49.40	0.83	0.91	1.59
50%O_2 + 50%CO_2	−0.16	13.44	24.58	1.51	0.86	0.87
	−0.08	13.49	41.97	1.37	0.86	0.96
	0	13.54	58.31	1.15	0.87	1.14
	0.08	13.67	67.52	0.78	0.91	1.69

Table 3. The fitted parameters in Fig. 3.
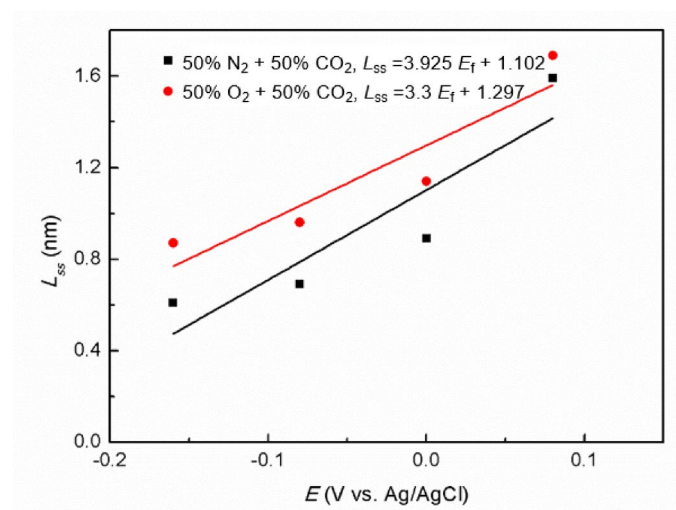
Fig. 4. Relationship between E_f and L_{ss} of Super 13Cr in 0.1 M NaCl solution in N_2/O_2 + CO_2 environment.

layer. Inner barrier layer, predominantly composed of Cr_2O_3 with a high point defects density, is crucial for protective properties. For Super 13Cr stainless steel, the composition of barrier layer is characterized as $Cr_{2-x}Fe_xO_3$, reflecting the higher Fe content relative to conventional austenitic stainless steels[45]. To maintain the stability of thickness and defect structure during M-S test, the reverse scan initiation potential was set to E_f, with low scan rate. The region above -0.4 V is selected to analysis the semiconductor properties of passive films to avoid alterations in the barrier layer properties at lower reverse scan potentials. Figure 5 presents the M-S results, demonstrating n-type under both experimental conditions, consistent with the potentiostatic polarization curve analysis (Fig. 2).

By linearly fitting the near-linear regions of the curves to extract the slopes, which facilitated the calculation of N_D and N_A via Eqs. (5) and (4). Across both the 50% O_2 + 50% CO_2 and 50% N_2 + 50% CO_2 environments, the higher E_f means the lower N_D. The trend is indicative of a reduced density of point defects, which is attributed to the annealing effect of anodic polarization[46], which is known to eliminate certain point defects. A decrease in N_D is beneficial as it mitigates the propensity for film rupture and pitting initiation. Thus, O_2-enriched environment (50% O_2 + 50% CO_2) improves the passive film stability by diminishing point defects density, thereby reducing film rupture risk.

The dependence of donor concentration (N_D) on E_f was characterized using an exponential function[47], as illustrated in Eq. (5). The parameters ω_1, ω_2, and b were determined through the exponential fitting of the N_D-E_f curve, with the results depicted in Fig. 6.

$$N_D = \omega_1 exp\left(-bE_f\right) + \omega_2 \tag{5}$$

The fitting outcomes are presented in Table 4. The relationship between ω_2 and the diffusion coefficient (D_0) of point defects is delineated by Eq. (6), which is pivotal for understanding the mobility of defects within the passive film[43].

$$D_0 = -\frac{J_0}{2K\omega_2} = -\frac{J_0 RT}{2F\varepsilon_L\omega_2} \tag{6}$$

$$J_0 = -\frac{i_{ss}}{2e} \tag{7}$$

The steady-state flux of point defects (J_0) and the constants, including the gas constant (R) and the Faraday constant (F), are integral to the calculation of the D_0, as defined by Eqs. (5) and (6). The D_0 for the passive film on Super 13Cr under both 50% O_2/N_2 + 50% CO_2 environments at various E_f could be determined utilizing

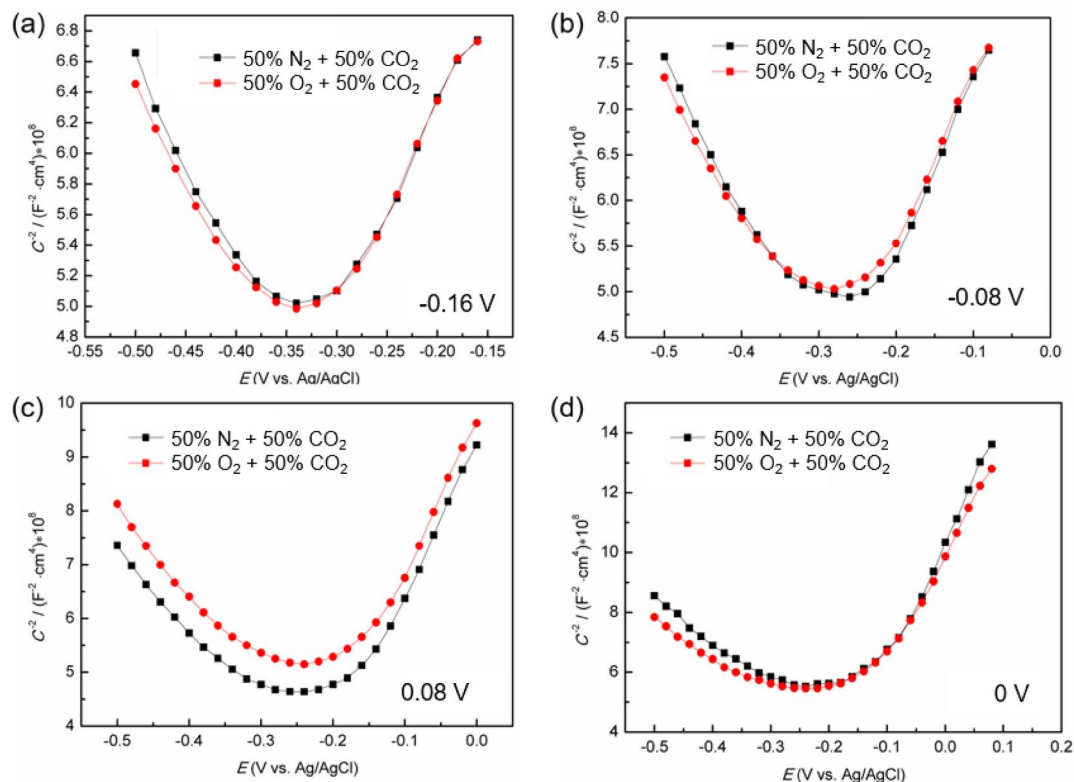**Fig. 5.** M-S curve of Super 13Cr in 0.1 M NaCl solution in N_2/O_2 + CO_2 environment after potentiostatic polarized at (**a**) -0.16 V, (**b**) -0.8 V, (**c**) 0 V, and (**d**) 0.8 V for 2 h.
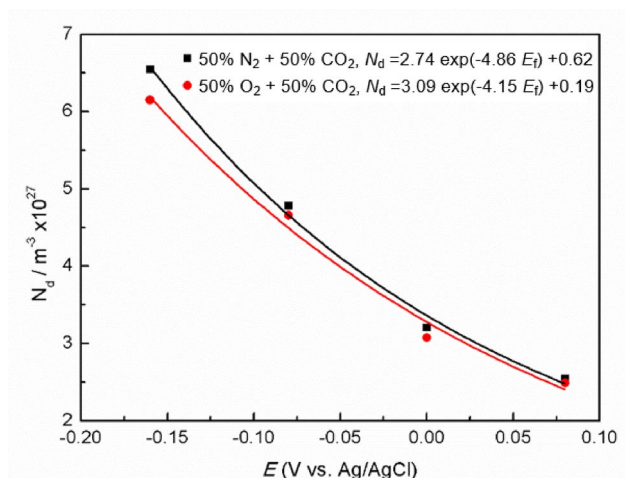
Fig. 6. Relationship of N_D and E_f in 0.1 M NaCl solution of Super 13Cr in N_2/O_2 + CO_2 environment.

Conditions	Parameters	E_f (V)	i_{ss} (10^{-6} A·cm^{-2})	D_0 (10^{-16} cm^2·s^{-1})
50%N_2 + 50%CO_2	ω_1 = 2.74 ω_2 = 0.62 b=−4.86	−0.16	2.475	2.46
		−0.08	2.628	2.61
		0	2.551	2.54
		0.08	2.398	2.38
50%O_2 + 50%CO_2	ω_1 = 3.09 ω_2 = 0.19 b=−4.15	−0.16	2.475	6.69
		−0.08	2.551	6.90
		0	2.628	7.10
		0.08	2.475	6.69

Table 4. Calculate parameters of super 13Cr under different E_f of 0.1 M NaCl in N_2/O_2 + CO_2 environment.
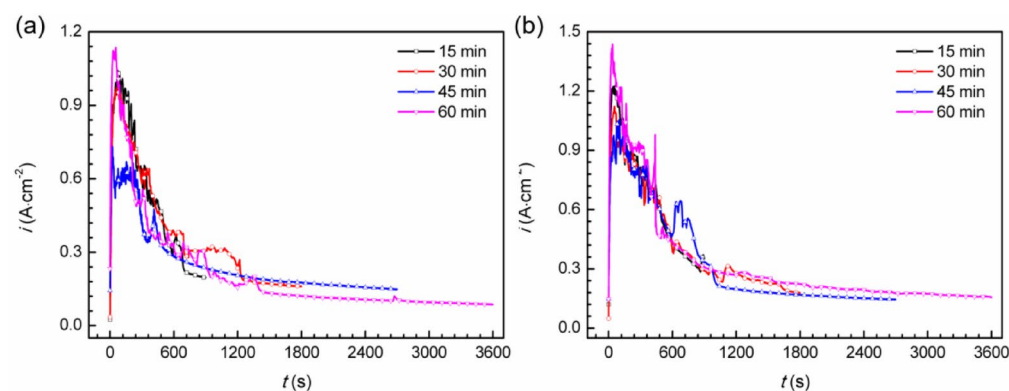
Fig. 7. Potentiostatic polarization curves of Super 13Cr at 0.75 V, (**a**) N_2 + CO_2 (**b**) O_2-CO_2 environment.

the equations with the established parameters. Our findings align with the reported D_0 values for the passive films on carbon steel in borate buffer solution as studied by Cheng et al.[48], and for 316 L stainless steel in similar solutions, as researched by Feng et al.[49], in terms of the order of magnitude. The consistency validates our experimental approach and supports the reliability of our results. In conclusion, as detailed in Table 4, O_2 significantly influences passive film characteristics by reducing film rupture propensity and enhancing the overall corrosion resistance of passive film via reducing point defects density.

Artificial pitting tests
An artificial pitting electrode was employed to potentiostatic anodically polarize the samples at potential of 0.75 V for varying durations (15, 30, 45 and 60 min), as depicted in Fig. 7. At the start of the polarization process, the current density surpassed 1 A·cm^{-2}, indicating the initiation of stable pitting due to the high polarization
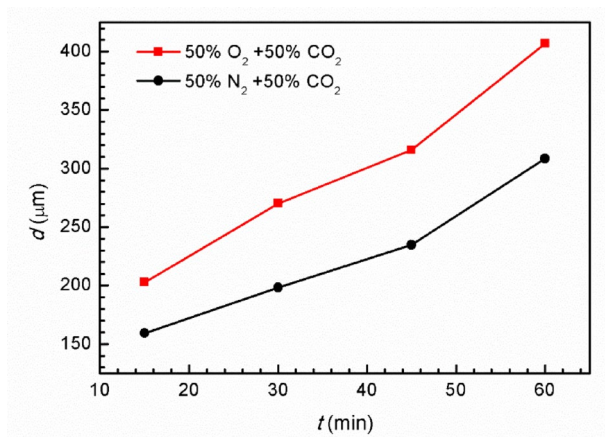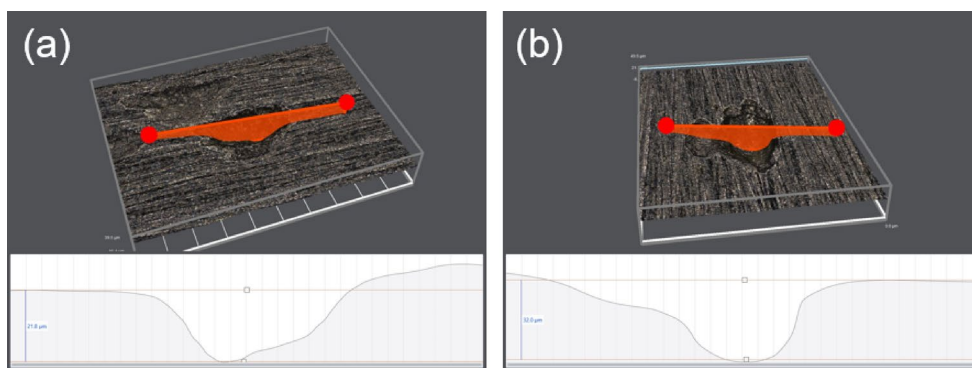
Fig. 8. Pit depth (d) calculated based on Eq. (8).

Fig. 9. Super depth of field microscope images of Super 13Cr stainless steel in (**a**) $N_2 + CO_2$ and (**b**) $O_2 + CO_2$ environment.

potential applied. During polarization, the current density decreased and eventually reached a steady state. The observed trend is attributed to the progressive formation of $FeCl_2$ salt layer at the base of the artificial pitting electrode. As the pit deepened, the rate-controlling step for stable pitting propagation shifted from activation-controlled to diffusion-controlled. The stabilization of the current density coincided with its approach to the limiting diffusion current density (i_L) value.

Utilizing Faraday's law, the depth of artificial pitting on Super 13Cr stainless steel was determined. The calculation is predicated on Eq. (8), wherein Z, representing the molar mass of Super 13Cr (55.8 g·mol^{-1}). n (= 2.16), corresponding to the average valence state of the cations. Additionally, ρ, the average density of Super 13Cr, is specified as 7.85 g·cm^{-3}. The outcomes of these calculations are graphically represented in Fig. 8.

$$d = \frac{Z}{nF\rho} \int i\,dt \qquad (8)$$

Figure 8 demonstrates that the depth of artificial pitting on the Super 13Cr stainless steel electrode linearly increases with potentiostatic anodic polarization time, suggesting that O_2 enhances the anodic dissolution process during the steady-state pitting.

Additionally, Fig. S1 presents the measured pitting depths on the artificial pitting electrode of Super 13Cr after various polarization durations. These measurements closely match the depths calculated using Faraday's law, with discrepancies within an acceptable error margin of 15%. Figure 9 shows the super depth of field microscope images of Super 13Cr after constant-current anode polarization (1 mA/cm^2) for 1 h in both environments. Large pits were observed in both environments, but the pit on Super 13Cr in the $O_2 + CO_2$ environment had a larger diameter and greater depth, consistent with the results obtained from Eq. (8). Moreover, the accumulation of corrosion products on the surface was not observed in either environment, as reported in the literature[50,51], indicating that Cl^- inhibited the formation of $FeCO_3$.

Figure 10 presents the data of the cathodic scan subsequent to the establishment of steady-state pitting growth under potentiostatic anodic polarization at 0.75 V for varying durations. At the start of the scan, the Super 13Cr surface is covered with $FeCl_2$ salt film, which controls the anodic dissolution rate through diffusion of Fe^{2+}, maintaining a stable current density (i_L). As the polarization potential progressively diminishes, the $FeCl_2$ salt
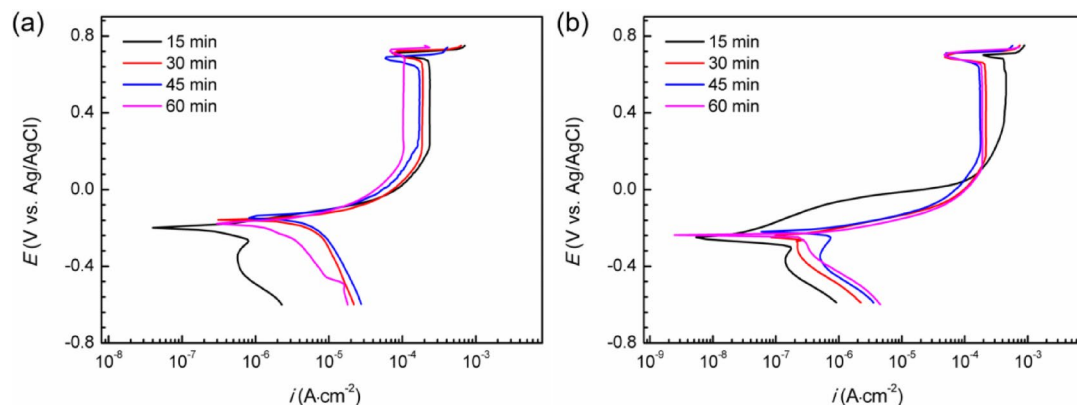
Fig. 10. Cathodic back sweep curves of Super 13Cr after potentiostatic polarization at 0.75 V, (**a**) $N_2 + CO_2$; (**b**) $O_2 + CO_2$ environment.
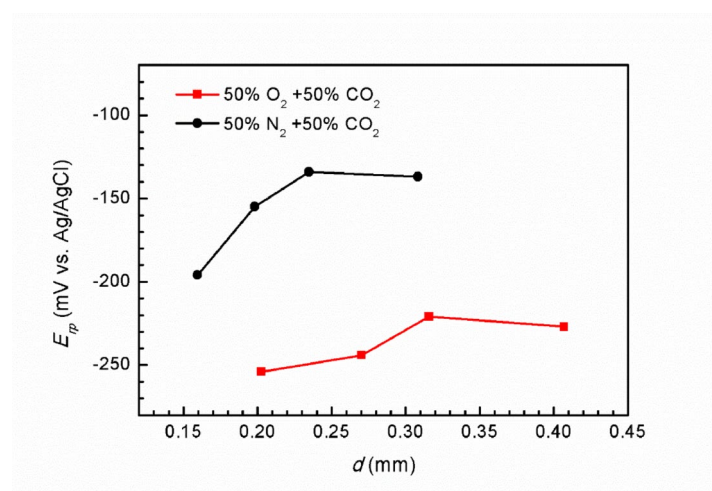

Fig. 11. E_{rp} of Super 13Cr in $N_2/O_2 + CO_2$ environment.

film on the Super 13Cr stainless steel dissolves, resulting in a significant drop in current density. The potential at which the transition occurs signifies the cessation of steady-state pitting, is defined as the repassivation potential (E_{rp}).

Figure 11 depicts the relationship between the E_{rp} and d for Super 13Cr stainless steel in two distinct environments. In each environment, E_{rp} initially increases with increasing pitting depth, followed by stabilization. The trend is associated with the steady-state pitting growth process, during which the anodic charge within the pits accumulates. Once a critical anodic charge is discharged, E_{rp} becomes independent of pitting depth, indicating a dynamic equilibrium between dissolution and repassivation[52]. In the 50% $N_2 + 50\%$ CO_2 environment, the E_{rp} of Super 13Cr stainless steel stabilizes at approximately -0.13 V. Conversely, in the 50% $O_2 + 50\%$ CO_2 environment, the E_{rp} is notably lower, at about -0.22 V. The reduction in E_{rp} in the presence of O_2 suggests a reduced capacity for repassivation in Super 13Cr stainless steel after the onset of stable pitting. The observation is consistent with preliminary insights from the Fig. 1.

The pitting stability product $(i \cdot x)_{saltfilm}$, which represents pitting corrosion stability under salt layer condition on metal surface, can be calculated using Eq. (9) as follows[53].

$$i_L d = nFD\Delta C = (i \cdot x)_{saltfilm} \qquad (9)$$

where D signifies the diffusion coefficient, and ΔC represents the concentration difference of metal cations between pit bottom and bulk solution. Figure 12 illustrates the relationship between the i_L and $1/d$ for Super 13Cr stainless steel. An inverse relationship is observed, with i_L decreasing as d increases, signifying that the anodic dissolution during the steady-state pitting process is predominantly governed by the diffusion. For environments with identical pitting depths, the higher i_L values in the 50% $O_2 + 50\%$ CO_2 environment suggests that O_2 enhances the diffusion kinetics. The linear correlation between i_L and $1/d$ implies that the product $i_L \cdot d$ is constant. Linear regression analysis of i_L versus $1/d$ yields products of 0.47 A·m^{-1} for 50% $O_2 + 50\%$ CO_2
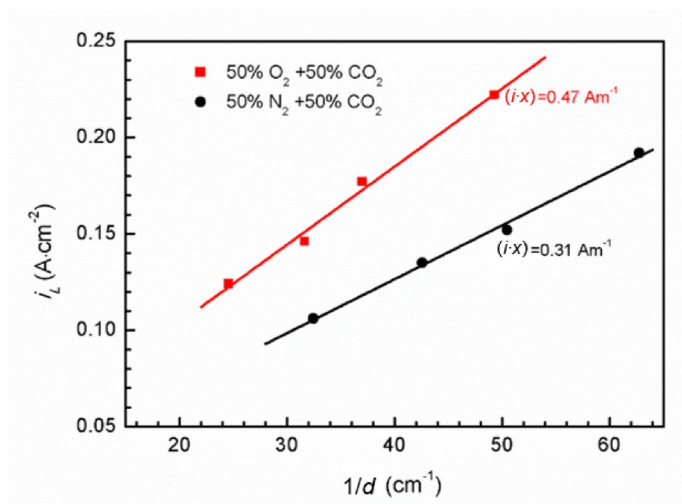
Fig. 12. Relation between i_L and $1/d$ in 0.1 M NaCl solution of Super 13Cr in $N_2/O_2 + CO_2$ environment.
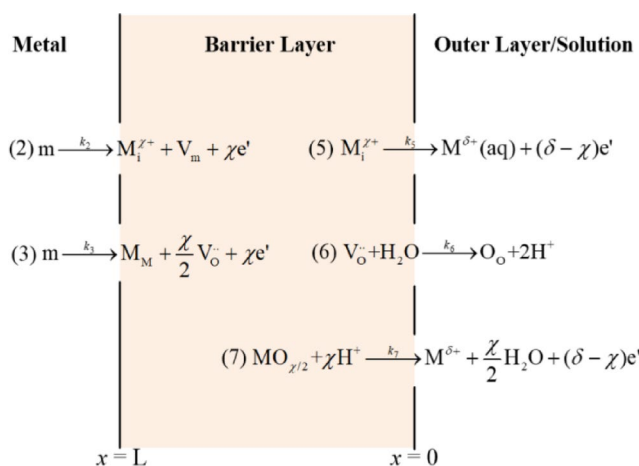

Fig. 13. Reaction diagram of N-type semiconductor passivation film based on PDM.

environment and 0.31 A·m^{-1} for the 50% N_2 + 50% CO_2 environment. According to Eq. (9), the product $i_L \cdot d$ is equivalent to the pitting stability product $(i \cdot x)_{saltfilm}$.

In accordance with Burstein's pitting corrosion theory[54], the pitting stability product $i \cdot a$ remains constant during the steady-state pitting phase, with the decisive threshold for the transition from metastable to stable pitting ranging from 0.3 to 0.6 A·m^{-1}. Our experimental findings align with the theoretical framework. The increased pitting stability product $(i \cdot x)_{saltfilm}$ for Super 13Cr in 50% O_2 + 50% CO_2 condition indicates that O_2 raises the threshold for the metastable pitting stability product $i \cdot a$ to reach the critical value necessary for the transition to stable pitting. The phenomenon also rationalizes the observation of higher pitting potential (E_b) in the 50% O_2 + 50% CO_2 environment, as depicted in Fig. 1.

Discussion
O$_2$ promotes passivation film densification
Figure 13 illustrates the reaction mechanism of n-type passive film, as proposed by the PDM[33]. The diagram shows atomic-scale reactions at lattice points within the passive film's crystal structure, particularly at matrix/barrier layer interface (m/bl) and the barrier/outer layer (solution) interface (bl/ol). In p-type semiconductor films, reactions (1) $M + V_M^{x'} \rightarrow M_M + V_M + xe'$ and (4) $M_M \rightarrow M^{x+} + V_M^{x'}$ characterize the behavior of metal vacancies $V_M^{x'}$. In contrast, for n-type semiconductors, the primary point defects are oxygen vacancies (V_o) and metal interstitial ions (M_i^{x+}), rendering reactions (1) and (4) inapplicable. The reactions depicted in Fig. 13 are as follows:

Reaction (2) and Reaction (5) signify the generation of metal interstitial ions and the entry into bulk solution, respectively. Reaction (3) and (6) portray the creation of V_o at m/bl and the filling through the capture of oxygen ions from H_2O at the bl/ol. Reaction (7) illustrates the dissolution process of the oxide film at the bl/ol, producing metal cations and H_2O. Here, m denotes metal atoms, V_m represents metal atom vacancies, $M^{\delta+}(aq)$
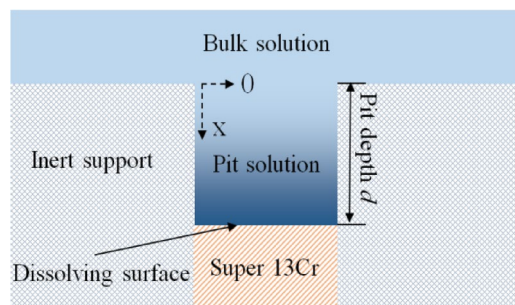
Fig. 14. Geometry of artificial pit electrode based on Galvele local acidification model.

refers to metal cations in the solution, M_M indicates metal cations situated at the lattice points of the passive film, O_O signifies oxygen ions at the lattice points, and $MO_{\chi/2}$ represents stoichiometric oxide passive films.

In the $N_2/O_2 + CO_2$ environment, the barrier layer on Super 13Cr exhibits characteristics of an n-type semiconductor, with predominant point defects being V_O and iron interstitial ions (Fe_i^{2+}). Given the larger ionic radius of Fe compared to O, Fe_i^{2+} requires more activation energy to penetrate the passive film barrier layer than V_O. The latter, acting as charge carriers, exhibit higher mobility within the passive film. Consequently, across both environments, V_O emerges as the dominant point defect. In $O_2 + CO_2$ condition, reaction (6) not only annihilates V_O at the bl/ol but also facilitates the adsorption of oxygen from solution into V_O, following the reaction $V_O + O_2 \rightarrow O_O + O$. The process accelerates the annihilation of V_O. Additionally, O_2 enhance D_0 of point defects, enabling V_O to diffuse more readily from m/bl to bl/ol. Furthermore, at equivalent film-forming potentials, the generation rate of V_O at m/bl via the reaction $Cr \rightarrow Cr_{Cr} + \frac{3}{2}V_O + 3e'$ remains consistent[55], indicating that the rate of V_O generation is invariant regardless of O_2 presence in the CO_2 environment. Collectively, these findings suggest that in O_2-enriched environments, V_O are more prone to diffusion and annihilation at the bl/ol, thereby enhancing passivation performance.

O_2 promotes the expansion of steady-state pitting

Once stable pitting corrosion is initiated in stainless steel, the corrosion process within the pit continues due to the creation of a localized, aggressive, and autocatalytic corrosive environment. A key parameter for assessing the intensity of the localized environment is the pH within the pit. Galvele's local acidification model[56–58] posits a mass transfer process limited to ionic diffusion, neglecting electromigration and convective effects, thereby simplifying the scenario to one-dimensional steady-state diffusion, as shown in Fig. 14. The hydrolysis of Fe^{2+}, resulting from anodic metal dissolution, is assumed to proceed via a single step reaction. From the local acidification model, Eq. (10) is derived, which includes the following relationships: $D_{Fe^{2+}}$ represents the diffusion coefficient of Fe^{2+}, $C_{Fe^{2+}}$ denotes the saturated solubility of $FeCl_2$, quantified at 4.2 M, D_{H+} is the diffusion coefficient of H^+, C_{H+} signifies the concentration of H^+ at the base of pit, with local pH defined as the negative logarithm of C_{H+}, $i_L \cdot d$ corresponds to the pitting stability product at the inception of stable pitting, x_1 defines the boundary condition at $d = 0$, reflecting the product of the C_{H+} and D_{H+}.

$$D_{Fe^{2+}} \cdot C_{Fe^{2+}} + D_{H+} \cdot C_{H+} = \frac{i_L d}{nF} + x_1 \qquad (10)$$

For Super 13Cr stainless steel featuring a $FeCl_2$ salt film at the base of artificial pits, metal anodic dissolution occurs during the steady-state pitting. The resultant Fe^{2+} undergo one-dimensional steady-state diffusion within the pit channel, extends to a depth of d. The concentrations of relevant ions comply with the conditions defined by Eq. (9). Given that the pH values of the bulk solution are identical in both environments, the boundary condition x_1 remains consistent. The pitting stability product $i_L \cdot d$ at the base of the artificial pits on Super 13Cr stainless steel is directly proportional to the C_{H+} at pit bottom and inversely proportional to local pH. It has been established that in the 50% O_2 + 50% CO_2 environment, the $i_L \cdot d$ value (0.47 A·m^{-1}) on Super 13Cr is higher than that in the 50% N_2 + 50% CO_2 environment (0.31 A·m^{-1}). Consequently, the pH at the base of the artificial pits on Super 13Cr in the $O_2 + CO_2$ environment is lower, indicating a more aggressive local corrosive environment. The finding suggests that O_2 exacerbates the severity of the local environment within pits where stable pitting occurs on Super 13Cr stainless steel.

Conclusion

In the study, techniques such as cyclic potentiodynamic polarization, potentiostatic polarization, EIS, M-S analysis, and artificial pitting electrodes were employed to investigate the passive film properties of Super 13Cr in 0.1 M NaCl solution under $O_2/N_2 + CO_2$ environments at ambient temperature. The effects of O_2 on the passive film properties, the kinetic characteristics of steady-state pitting-repassivation behavior, and the underlying mechanisms were elucidated using the point defect model (PDM) and Galvele's local acidification theory. The findings reveal the mechanisms governing passivation performance and pitting growth kinetics, as summarized below:

1. Upon achieving a fully passivated state, O_2 promotes the development of the passive film, increasing its thickness, enhancing the D_0 and reduces the N_D, this diminishes the probability of film rupture and pitting initiation, thereby enhancing passivation performance.
2. During the transition process of metastable to stable pitting, O_2 lowers the metastable pitting stability product ($i \cdot a$) and raises the threshold for the transition. Specifically, the pitting stability product in the presence of a salt film, $(i \cdot x)_{saltfim}$, is increased. These dual effects inhibit the transformation to stable pitting.
3. In the stable pitting process, O_2 reduces the repassivation potential and increases both the i_L and $(i \cdot x)_{saltfim}$, leading to a decreased pH level at the base of the pit, creating a more aggressive local corrosive environment. Consequently, this results in greater pit depth and an accelerated pitting growth rate, which in turn weakens the repassivation capability of Super 13Cr.

Data availability

The datasets used and/or analysed during the current study available from the corresponding author on reasonable request.

References

1. Huang, S., Zhang, Y. & Sheng, J. J. Experimental investigation of enhanced oil recovery mechanisms of air injection under a low-temperature oxidation process: thermal effect and residual oil recovery efficiency. *Energy Fuels.* **32**, 6774–6781 (2018).
2. Cheng, W. & Han, B. Wellbore heat transfer model of multiple thermal fluid based on real gas state equation. *Acta Petrolei Sinica.* **36**, 1402 (2015).
3. Farag, W. A. & Helal, M. Exploring key aspects: structure, properties, production, and oil & gas applications of graphene and its nanoribbons – A comprehensive review. *Geoenergy Sci. Eng.* **231**, 212416 (2023).
4. Li, X. et al. Effect of extremely aggressive environment on the nature of corrosion scales of HP-13Cr stainless steel. *Appl. Surf. Sci.* **469**, 146–161 (2019).
5. Liu, W. et al. Failure analysis on fracture of S13Cr-110 tubing. *Eng. Fail. Anal.* **90**, 215–230 (2018).
6. Qi, W., Gao, Q., Zhao, Y., Zhang, T. & Wang, F. Insight into the stress corrosion cracking of HP-13Cr stainless steel in the aggressive geothermal environment. *Corros. Sci.* **190**, 109699 (2021).
7. Lu, Q. et al. Corrosion evolution and stress corrosion cracking of E690 steel for marine construction in artificial seawater under potentiostatic anodic polarization. *Constr. Build. Mater.* **238**, 117763 (2020).
8. Zhao, Y. et al. Investigation of the failure mechanism of the TG-201 inhibitor: promoting the synergistic effect of HP-13Cr stainless steel during the well completion. *Corros. Sci.* **166**, 108448 (2020).
9. Yue, X. et al. A thermodynamic and kinetic study of the formation and evolution of corrosion product scales on 13Cr stainless steel in a geothermal environment. *Corros. Sci.* **169**, 108640 (2020).
10. Zhao, Y. et al. A new high-efficiency experimental design for optimizing various flow velocities testing in extremely aggressive formation water. *Acta Metall. Sinica (English Letters).* **32**, 944–950 (2019).
11. Gao, M., Pang, X. & Gao, K. The growth mechanism of CO2 corrosion product films. *Corros. Sci.* **53**, 557–568 (2011).
12. Lei, X. et al. Impact of reversed austenite on the pitting corrosion behavior of super 13Cr martensitic stainless steel. *Electrochim. Acta.* **191**, 640–650 (2016).
13. Sunaba, T. et al. Influence of chloride ions on corrosion of modified martensitic stainless steels at high temperatures under a CO2 environment. *Corrosion* **70**, 988–999 (2014).
14. Fredriksson, W., Malmgren, S., Gustafsson, T., Gorgoi, M. & Edström, K. Full depth profile of passive films on 316L stainless steel based on high resolution HAXPES in combination with ARXPS. *Appl. Surf. Sci.* **258**, 5790–5797 (2012).
15. Wu, H. et al. Comparative study of the corrosion behavior of base metal and welded joint of Ti-6Al-3Nb-2Zr-1Mo alloy in the acidic chloride environment. *Corros. Sci.* **244**, 112649 (2025).
16. Abdel Salam, A., Elshabasy, A. & Elzawawy, M. Carrier line technique for downhole chemical injection in oil and gas industry; case study: El Hamra oil company. *Egypt. J. Petroleum.* **32**, 42–47 (2023).
17. Zarei, M., Eskandarzade, M., Babapoor, A. & Seyfaee, A. A review of recent advances and applications of inorganic coating for oil and gas pipe systems. *Surf. Coat. Technol.* **494**, 131339 (2024).
18. Mubarak, G., Verma, C., Barsoum, I., Alfantazi, A. & Rhee, K. Y. Internal corrosion in oil and gas wells during casings and tubing: challenges and opportunities of corrosion inhibitors. *J. Taiwan Inst. Chem. Eng.* **150**, 105027 (2023).
19. LIN, X. Q. et al. Characteristics of corrosion scale of 3Cr steel at high temperature and pressure in an O2 and CO2 environment. *Acta Phys. Chim. Sin.* **29**, 2405–2414 (2013).
20. Luo, S. et al. Stress corrosion cracking behavior and mechanism of super 13Cr stainless steel in simulated O2/CO2 containing 3.5 Wt% NaCl solution. *Eng. Fail. Anal.* **130**, 105748 (2021).
21. Li, K., Zeng, Y. & Luo, J. L. Corrosion of SS310 and alloy 740 in high temperature supercritical CO2 with impurities H2O and O2. *Corros. Sci.* **184**, 109350 (2021).
22. Bouhieda, S., Rouillard, F., Barnier, V. & Wolski, K. Selective oxidation of chromium by O 2 impurities in CO 2 during initial stages of oxidation. *Oxid. Met.* **80**, 493–503 (2013).
23. Brittan, A., Mahaffey, J., Adam, D. & Anderson, M. Mechanical and corrosion response of 316SS in supercritical CO2. *Oxid. Met.* **95**, 409–425 (2021).
24. Jang, H. & Kwon, H. In situ study on the effects of Ni and mo on the passive film formed on Fe–20Cr alloys by photoelectrochemical and mott–Schottky techniques. *J. Electroanal. Chem.* **590**, 120–125 (2006).
25. Fattah-Alhosseini, A., Soltani, F., Shirsalimi, F., Ezadi, B. & Attarzadeh, N. The semiconducting properties of passive films formed on AISI 316 L and AISI 321 stainless steels: A test of the point defect model (PDM). *Corros. Sci.* **53**, 3186–3192 (2011).
26. Soltis, J. Passivity breakdown, pit initiation and propagation of pits in metallic materials –. *Rev. Corros. Sci.* **90**, 5–22 (2015).
27. Lv, N. X. et al. *Influence of Oxygen Partial Pressure on the Passivation and Depassivation of Super 13Cr Stainless Steel in High Temperature and CO < sub > 2 rich Environment*14 (SCIENTIFIC REPORTS, 2024).
28. Naixin, Lv., et al. Influence of oxygen on metastable pitting behavior of super 13Cr stainless steel in CO2-saturated environment. *Vacuum* **232**, 113845 (2025).
29. Luo, H., Wang, X., Dong, C., Xiao, K. & Li, X. J. C. S. Effect of cold deformation on the corrosion behaviour of UNS S31803 duplex stainless steel in simulated concrete pore solution. *Corros. Sci.* **124**, 178–192 (2017).
30. Sasaki, K. & Burstein, G. T. The generation of surface roughness during slurry erosion-corrosion and its effect on the pitting potential. *Corros. Sci.* **38**, 2111–2120 (1996).
31. Wu, H. et al. Comparative study of stress corrosion cracking and corrosion-induced mechanical property degradation of 7050-T7451 aluminum alloy in chloride solution containing bisulfite. *Eng. Fail. Anal.* **167**, 109054 (2025).

32. Esmailzadeh, S., Aliofkhazraei, M. & Sarlak, H. J. P. M. P.C.o. Surfaces, interpretation of Cyclic potentiodynamic polarization test results for study of corrosion behavior of metals: A review. *Prot. Met. Phys. Chem. Surf.* **54**, 976–989 (2018).
33. Macdonald, D. D. The history of the point defect model for the passive State: A brief review of film growth aspects. *Electrochim. Acta.* **56**, 1761–1772 (2011).
34. Freire, L., Carmezim, M. J., Ferreira, M. G. S. & Montemor, M. F. The electrochemical behaviour of stainless steel AISI 304 in alkaline solutions with different pH in the presence of chlorides. *Electrochim. Acta.* **56**, 5280–5289 (2011).
35. Boissy, C., Alemany-Dumont, C. & Normand, B. EIS evaluation of steady-state characteristic of 316L stainless steel passive film grown in acidic solution. *Electrochem. Commun.* **26**, 10–12 (2013).
36. de Pauli, M. et al. Capacitance spectra extracted from EIS by a model-free generalized phase element analysis. *Electrochim. Acta.* **320**, 134366 (2019).
37. Li, J. et al. Enhancing the corrosion resistance of the epoxy coating using CaAl LDH intercalated with L-cysteine and its derivatives as a pigment on steel substrate. *Prog. Org. Coat.* **193**, 108527 (2024).
38. Zeng, H., Yang, Y., Zeng, M. & Li, M. Effect of dissolved oxygen on electrochemical corrosion behavior of 2205 duplex stainless steel in hot concentrated seawater. *J. Mater. Sci. Technol. -Shenyang-.* **66**, 177–185 (2021).
39. Yue, Y., Liu, C., Shi, P. & Jiang, M. J. C. E. Science, technology, passivity of stainless steel in sulphuric acid under chemical oxidation. *Corros. Eng. Sci. Technol.* **53**, 173–182 (2018).
40. Li, D. G., Wang, J. D., Chen, D. R. & Liang, P. Influences of pH value, temperature, chloride ions and sulfide ions on the corrosion behaviors of 316L stainless steel in the simulated cathodic environment of proton exchange membrane fuel cell. *J. Power Sources.* **272**, 448–456 (2014).
41. Meng, G. et al. Technology, effect of Cl – on the properties of the passive films formed on 316L stainless steel in acidic solution. *J. Mater. Sci. Technol.* **30**, 253–25 (2014).
42. Kim, Y. et al. Electrochemical analysis on the potential decay behavior of Fe-20Cr stainless steels in sulfuric acid solution. *Electrochim. Acta.* **266**, 1–6 (2018).
43. Vázquez, G. & González, I. Diffusivity of anion vacancies in WO3 passive films. *Electrochim. Acta.* **52**, 6771–6777 (2007).
44. Fattah-alhosseini, A. Passivity of AISI 321 stainless steel in 0.5 M H2SO4 solution studied by Mott–Schottky analysis in conjunction with the point defect model. *Arab. J. Chem.* **9**, S1342–S1348 (2016).
45. Brüesch, P., Müller, K., Atrens, A. & Neff, H. J. A. P. A. Corrosion of stainless steels in chloride solution: an XPS investigation of passive films. *Appl. Phys. A.* **38**, 1–18 (1985).
46. Wang, X. Z., Luo, H. & Luo, J. L. Effects of hydrogen and stress on the electrochemical and passivation behaviour of 304 stainless steel in simulated PEMFC environment. *Electrochim. Acta.* **293**, 60–77 (2019).
47. Meng, G. et al. Effect of microstructures on corrosion behavior of nickel coatings: (I) abnormal grain size effect on corrosion behavior. *J. Mater. Sci. Technol.* **31**, 1186–1192 (2015).
48. Cheng, Y. F., Yang, C. & Luo, J. L. Determination of the diffusivity of point defects in passive films on carbon steel. *Thin Solid Films.* **416**, 169–173 (2002).
49. Feng, Z., Cheng, X., Dong, C., Xu, L. & Li, X. Effects of dissolved oxygen on electrochemical and semiconductor properties of 316L stainless steel. *J. Nucl. Mater.* **407**, 171–177 (2010).
50. Zhang, S. et al. A study on the interaction between chloride ions and CO2 towards carbon steel corrosion. *Corros. Sci.* **167**, 108531 (2020).
51. Wang, L. et al. Optimizing the resistance of Cr-advanced steel to CO2 corrosion with the addition of Ni. *J. Mater. Res. Technol.* **32**, 97–111 (2024).
52. Srinivasan, J., McGrath, M. & J.o.T, R. J. A high-throughput artificial pit technique to measure kinetic parameters for pitting stability. *J. Electrochem. Soc.* **162**, C725 (2015).
53. Moayed, M. H. & Newman, R. C. Deterioration in critical pitting temperature of 904L stainless steel by addition of sulfate ions. *Corros. Sci.* **48**, 3513–3530 (2006).
54. Pistorius, P. (ed E. Burstein) Metastable pitting corrosion of stainless steel and the transition to stability. *Sciences* **341** 531–559 (1992).
55. M.R.E.D.M.J.E., Y. Z. U. Development of localized corrosion damage on low pressure turbine disks and blades: I. Passivity. *Acta* **69**, 1–11 (2012).
56. Galvele, J. R. J. Transport processes and the mechanism of pitting of metals. *J. O T E S.* **123**, 464 (1976).
57. Galvele, J. Transport processes in passivity breakdown—II. Full hydrolysis of the metal ions. *Corros. Sci.* **21**, 551–579 (1981).
58. Li, Y. & Xu, J. Differences in pitting growth kinetics between Zr60Ni25Al15 and Zr60Cu25Al15 metallic glasses exposed to a 0.6 M NaCl aqueous solution. *Corros. Sci.* **128**, 73–84 (2017).

Acknowledgements

Author contributions

Lv Naixin: experiments execution and analyzeFu Anqing: funding approval and methods Yu Haitao: sample preparation and electrochemical tests Zhang Gang : experimental executionWei Chenghua : experimental execution and figure analyzeWang Xia : software Xu Zhengyi: manuscript writing and revisingWang Yanqiu: experimental data analyse.

Declarations

Competing interests

The authors declare no competing interests.

Additional information

Publisher's note Springer Nature remains neutral with regard to jurisdictional claims in published maps and institutional affiliations.